されていくべきであるが，通常の照射技法では正常臓器の線量を十分に低下させられない場合も多く，有害事象の増加の恐れもあり，3D-CRTもしくはIMRTという技法を使用した上で，十分に注意して行われるべきと考えられる。

5 有害事象とその対策

放射線治療の有害事象は，照射中から照射終了後3カ月以内にかけて急性期のものとそれ以降の晩期のものに大きく分けられる。外部照射の場合一般に問題になるのは晩期の有害事象である。前立腺癌外部照射の場合の有害事象は消化管，尿路，性機能，およびその他に分類することができる。

1）急性期の有害事象

急性期の有害事象としては，頻尿，排尿時痛，下痢，肛門部痛などがある。いずれも軽症で治療終了後1～4週以内で改善するが，まれに重症化することもある。通常最も問題になるのは尿路障害（主に頻尿）である。尿路は前立腺の中を貫通するために，照射技法で緩和することは困難である。軽症なものは特に治療を必要としないが，尿路刺激症状の中等度以上のものにはα1ブロッカーの投与が有効なことがある[14]。場合に応じて鎮痛剤も有効である。直腸刺激症状の頻度および程度は照射技法に依存する。中等度以上のものに対しては，止痢剤の投与を行う。肛門部痛も照射野の設定法に依存しており，この症状がある時には照射野を確認し，必要以上に下方まで設定されている場合には，必要な範囲に変更する。そのほか時に尿路出血，直腸出血が生じることがあるが，いずれも軽症で，一過性のことがほとんどである。

2）晩期有害事象

(1) 消化管

晩期有害事象で最も問題になるのは直腸出血である。照射される線量や照射野および評価基準の違いなどによりその頻度には0％から30％以上と大きな幅がある。

従来の外部照射から3D-CRT，さらにIMRTと技術の進歩に伴って直腸障害の頻度を低く抑えることができる，あるいは頻度を同等に保ったまま腫瘍に対する線量を増加させることができるとする報告は多く[15][16]，PSAでの効果判定が行われる時代になっても根治性をより高めつつ，低い発生頻度で治療が施行されつつある。

ちなみに当科で3D-CRTを使用し，前立腺癌に72Gy以上投与した症例のgrade II以上の直腸出血の割合は約6％であった。

直腸出血の治療はまず発生予防であり，できる限り直腸の70Gy以上照射さ

れる体積を少なくすることが肝要である。また直腸粘膜の便塊による刺激を回避すべく，定期排便についての患者教育も重要である。さらに実際に発生した場合には，緩下剤，止血剤等の投与，貧血の是正，TPNの施行と可及的に保存的治療を行うが，難治性の場合は人工肛門の造設も検討する。

(2) 尿路

尿路系の晩期有害事象は急性期にみられる頻尿や排尿痛などの頻度に比べて，その頻度は一般に低い。具体的な症状としては頻尿，尿道狭窄，尿失禁がある。尿路障害についても照射技術の向上による有害事象の減少は報告されている[17]。

治療は一般的に対症的である。予防法としては膀胱への70Gy以上照射される体積を可及的に低く抑えることが肝要である。

(3) 性機能

性機能の評価は照射後長期にわたって行う必要がある。一般にいわれていることは手術療法と比べて放射線治療では最初の1年間は性機能の回復傾向が似ているが，手術では1年後も回復傾向がみられるのに対し，放射線療法では1年以降はむしろ性機能の低下傾向がみられることである[18]。さらにホルモン剤の使用が状況を複雑にしている。尿道球部への線量が大きいとインポテンスになるという報告もある。この点は最近の3D-CRTおよびIMRT等の照射技術により，同部の線量を低減できるので，留意すべきである。治療はsildenafil（バイアグラ）等の投与，その他精神的なカウンセリングも有効なことがある。

(4) その他

頻度的には少ないものの，外部照射後の有害事象として，大腿骨頭壊死もしくは頸部骨折がみられることがある。大腿骨頭へは50Gyを超えないよう注意する必要がある。

また放射線治療後の発癌については，種々の報告があるが，1%程度の報告が多い。前立腺癌の患者の年齢が比較的高齢であることから，放射線二次発癌はあまり問題とならないことが多いが，今後若年の患者が増えれば，増えていく可能性はある。特に予防手段はないが，原病の経過観察を定期的に行っていれば，出現しても早期に発見され，根治させられる可能性は高まる。

●文　献

1) Kuban DA et al：Prostate-specific antigen for pretreatment prediction and posttreatment evaluation of outcome after definitive irradiation for prostate cancer. Int J Radiat Oncol Biol Phys 32：307-316, 1995

2) Kupelian PA et al：Comparison of the efficacy of local therapies for localized prostate cancer in the prostate-specific antigen era；a large single-institution experience with radical prostatectomy and

external-beam radiotherapy. J Clin Oncol 20 : 3376-3385, 2002
3) Kupelian PA et al : Radical prostatectomy, external beam radiotherapy <72 Gy, external beam radiotherapy > or =72 Gy, permanent seed implantation, or combined seeds/external beam radiotherapy for stage T1-T2 prostate cancer. Int J Radiat Oncol Biol Phys 58 : 25-33, 2004
4) Roach M 3rd et al : Radiation Therapy Oncology Group 9413. Phase III trial comparing whole-pelvic versus prostate-only radiotherapy and neoadjuvant versus adjuvant combined androgen suppression ; Radiation Therapy Oncology Group 9413. J Clin Oncol 21 : 1904-1911, 2003
5) Liauw SL et al : Salvage radiotherapy for biochemical failure of radical prostatectomy ; a single-institution experience. Urology 61 : 1204-1210, 2003
6) Pollack A et al : External beam radiotherapy dose response characteristics of 1127 men with prostate cancer treated in the PSA era. Int J Radiat Oncol Biol Phys 48 : 507-512, 2000
7) Hanks GE et al : Dose selection for prostate cancer patients based on dose comparison and dose response studies. Int J Radiat Oncol Biol Phys 46 : 823-832, 2000
8) Pollack A et al : Prostate cancer radiation dose response ; results of the M.D. Anderson phase III randomized trial. Int J Radiat Oncol Biol Phys 53 : 1097-1105, 2002
9) Jani AB et al : Impact of hormone therapy when combined with external beam radiotherapy for early-stage, intermediate-, or high-risk prostate cancer. Am J Clin Oncol 26 : 382-385, 2003
10) Zelefsky MJ et al : High-dose intensity modulated radiation therapy for prostate cancer ; early toxicity and biochemical outcome in 772 patients. Int J Radiat Oncol Biol Phys 53 : 1111-1116, 2002
11) Pilepich MV et al : Androgen suppression adjuvant to definitive radiotherapy in prostate carcinoma--long-term results of phase III RTOG 85-31. Int J Radiat Oncol Biol Phys 61 : 1285-1290, 2005
12) Bolla M et al : Long-term results with immediate androgen suppression and external irradiation in patients with locally advanced prostate cancer (an EORTC study) ; a phase III randomised trial. Lancet 360 : 103-106, 2002
13) Roach M 3rd et al : Predicting long-term survival, and the need for hormonal therapy ; a meta-analysis of RTOG prostate cancer trials. Int J Radiat Oncol Biol Phys 47 : 617-627, 2000
14) Prosnitz RG et al : Tamsulosin palliates radiation-induced urethritis in patients with prostate cancer ; results of a pilot study. Int J Radiat Oncol Biol Phys 45 : 563-566, 1999
15) Dearnaley DP et al : Comparison of radiation side-effects of conformal and conventional radiotherapy in prostate cancer ; a randomised trial. Lancet 353 : 267-272, 1999
16) Zelefsky MJ et al : High-dose intensity modulated radiation therapy for prostate cancer ; early toxicity and biochemical outcome in 772 patients. Int J Radiat Oncol Biol Phys 53 : 1111-1116, 2002
17) Schultheiss TE et al : Incidence of and factors related to late complications in conformal and conventional radiation treatment of cancer of the prostate. Int J Radiat Oncol Biol Phys 32 : 643-649, 1995
18) Litwin MS et al : Sexual function and bother after radical prostatectomy or radiation for prostate cancer ; multivariate quality-of-life analysis from CaPSURE. Cancer of the Prostate Strategic Urologic Research Endeavor. Urology 54 : 503-508, 1999

Int. J. Radiation Oncology Biol. Phys., Vol. 66, No. 1, pp. 271–278, 2006

0360-3016/06/$–see front matter

ELSEVIER

doi:10.1016/j.ijrobp.2006.04.044

PHYSICS CONTRIBUTION

DEVELOPMENT OF A FOUR-DIMENSIONAL IMAGE-GUIDED RADIOTHERAPY SYSTEM WITH A GIMBALED X-RAY HEAD

YUICHIRO KAMINO, M.S.,* KENJI TAKAYAMA, M.D.,*† MASAKI KOKUBO, M.D., PH.D.,‡ YUICHIRO NARITA, PH.D.,† ETSURO HIRAI, PH.D.,* NORIYUKI KAWAWDA, B.S.,* TAKASHI MIZOWAKI, M.D., PH.D.,† YASUSHI NAGATA, M.D., PH.D.,† TAKEHIRO NISHIDAI, PH.D.,§ AND MASAHIRO HIRAOKA, M.D., PH.D.†

*Mitsubishi Heavy Industries, Ltd., Tokyo, Japan; †Department of Radiation Oncology and Image-applied Therapy, Graduate School of Medicine, Kyoto University, Kyoto, Japan; ‡Institute of Biomedical Research and Innovation, Kobe, Japan; §Kyoto College of Medical Technology, Kyoto, Japan

Purpose: To develop and evaluate a new four-dimensional image-guided radiotherapy system, which enables precise setup, real-time tumor tracking, and pursuit irradiation.

Methods and Materials: The system has an innovative gimbaled X-ray head that enables small-angle (±2.4°) rotations (pan and tilt) along the two orthogonal gimbals. This design provides for both accurate beam positioning at the isocenter by actively compensating for mechanical distortion and quick pursuit of the target. The X-ray head is composed of an ultralight C-band linear accelerator and a multileaf collimator. The gimbaled X-ray head is mounted on a rigid O-ring structure with an on-board imaging subsystem composed of two sets of kilovoltage X-ray tubes and flat panel detectors, which provides a pair of radiographs, cone beam computed tomography images useful for image guided setup, and real-time fluoroscopic monitoring for pursuit irradiation.

Results: The root mean square accuracy of the static beam positioning was 0.1 mm for 360° of O-ring rotation. The dynamic beam response and positioning accuracy was ±0.6 mm for a 0.75 Hz, 40-mm stroke and ±0.4 mm for a 2.0 Hz, 8-mm stroke. The quality of the images was encouraging for using the tomography-based setup. Fluoroscopic images were sufficient for monitoring and tracking lung tumors.

Conclusions: Key functions and capabilities of our new system are very promising for precise image-guided setup and for tracking and pursuit irradiation of a moving target. © 2006 Elsevier Inc.

IGRT, 4D-IGRT, Organ motion compensation, Pursuit irradiation, CBCT.

INTRODUCTION

Image-guided radiotherapy (IGRT) is a key method for precise targeting for radiotherapy. There are two major functions of IGRT: one is for initial setup in each fraction (interfraction), and the other is for motion compensation during fraction (intrafraction).

For precise initial setup, electronic portal imaging devices (EPID) were developed in the 1990s (1), which enabled verification by means of bony structures or fiducial markers. Off-board or on-board kilovoltage (kV) radiograph and fluoroscopy devices were then introduced that provided better image quality than EPID. CyberKnife (2) and ExacTrac (3) have an off-board stereoscopic kV-radiography system combined electronically with a linear accelerator (LINAC). More recently, Jaffray *et al.* (4) mounted a set of kV X-ray tubes and an image detector on the gantry of a LINAC. It is also useful to have a computed tomography (CT) scanner in the treatment room because of the advantage of volumetric imaging, which enables soft-tissue verification as well as conventional verification using boney or fiducial markers (5). An on-board cone beam computed tomography (CBCT) is highly desirable because three-dimensional (3D) imaging data can be acquired at one time for verification. Jaffray *et al.* (6) developed a CBCT function using an on-board kV imaging subsystem. Similar systems have been developed and evaluated clinically (7, 8). Megavoltage (MV) CBCT systems (9, 10) and an MV CT system (11) have also been developed.

Reprint requests to: Daisaku Horiuchi, MHI Medical Systems, Inc., Mita-Nitto-Dai Building, 5th Floor, 11-36 Mita 3-Chome, Minato-Ku Tokyo, 108-0073 Japan. E-mail: daisaku_horiuchi@mhi.co.jp

Supported by New Energy and Industrial Technology Development Organization (NEDO) of Japanese government as Key Technology Research Promotion (Grant No. 05000942-0).

Acknowledgments—We are thankful for the assistance of Mr. Ichiro Yamashita of Mitsubishi Heavy Industries, Ltd., with accelerator technology. We are also thankful for the assistance of Dr. Tokihiro Yamamoto of the Graduate School of Medicine, Osaka University, in the monitoring dose evaluation.

Received Nov 26, 2005, and in revised form April 13, 2006. Accepted for publication April 14, 2006.

Compensation for intrafraction respiratory organ motion is clinically a most challenging problem. There have been two categories of study on organ motion compensation. One is real-time monitoring or estimation of the position and shape of the target, and the other is the method of dose delivery to the target that changes in position and shape.

As an approach to real-time monitoring, Shimizu *et al.* (12) introduced off-board stereo fluoroscopes to observe internal fiducial markers in real time. Berbeco *et al.* (7) proposed an integrated radiotherapy imaging system (IRIS) with an on-board integrated imaging subsystem. Their system had two sets of kV X-ray tubes and flat panel detectors (FPDs) on the gantry of the LINAC to provide stereoscopic fluorography for real-time observation of the target or fiducial marker; it also had stereoscopic radiography and a CBCT for setup. Keall (13) proposed the use of four-dimensional CT (4D-CT) images in the preparation phase to estimate the real tumor position during beam delivery. Neicu *et al.* (14) proposed use of the average tumor trajectory determined before beam delivery with real-time verification monitoring with IRIS. Schweikard *et al.* (15, 16) proposed a combination of real-time monitoring of an internal fiducial marker and an external infrared marker. Keall *et al.* (17) proposed real-time monitoring of internal fiducial markers with EPID during irradiation.

A popular approach to dose delivery is gated irradiation (18–21) in which the treatment beam is fixed in space and gated to turn on only when the target, fiducial marker, or other surrogate signal comes into the preplanned area. Alternatively, a small LINAC head follows the target motion on a robotic arm (15, 16, 22) to provide pursuit irradiation. Dynamic control of the collimation aperture has also been studied as an advanced derivative of the dynamic multileaf collimator for pursuit irradiation (14, 23–26).

We are developing an innovative 4D-IGRT system with a unique gimbaled X-ray head, which provides both image-guided precise setup capability and pursuit irradiation. In this article the concept and design of the system and the results of preliminary system evaluation are presented.

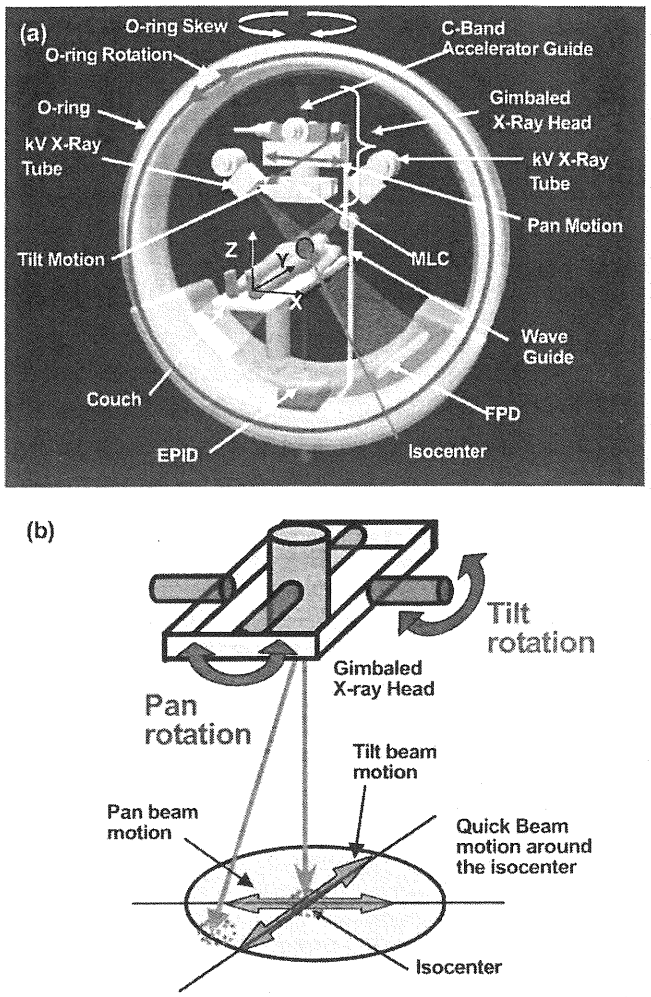

Fig. 1. (a) The gimbaled X-ray head is mounted on the O-ring with two kV X-ray tubes, two flat panel detectors (FPDs), and an electronic portal imaging device (EPID). The O-ring can be rotated 360° around the isocenter and can be skewed ±60° around its vertical axis. The couch has motion in X, Y, and Z. The waveguide provides microwave energy to the X-ray head. The X-ray head has a multileaf collimator to control dose distribution. (b) The pan and tilt rotations provide a precise and quick beam motion around the isocenter.

METHODS AND MATERIALS

Concept

The system has two modes of operation. One is the static treatment mode, which is not accompanied by dynamic pursuit beam motion. In the static treatment mode, the beam will be deflected from the machine isocenter to compensate for a small displacement of the target from the machine isocenter, if necessary. In this mode, the treatment beam can be gated to compensate for organ motion. The other mode is the dynamic treatment mode. In this mode, the treatment beam is deflected dynamically and pursues the target in real time for the organ motion compensation.

The system concept is shown in Fig. 1. The system has an isocenter at the mechanical center of the O-ring. The X-ray head is supported on the gimbals and can be driven to rotate in pan and tilt directions. The gimbaled X-ray head is supported on the O-ring. The gimbaled X-ray head can be rotated 360° on the O-ring, and this ring rotation enables a planar port selection. The O-ring can be skewed around its vertical axis, and this skew provides both a noncoplanar beam angle selection and a yaw angle correction in the setup.

In the static treatment mode, the pan and tilt motions of the X-ray head compensate for mechanical distortion caused mainly by the weight of the X-ray head, and the beam is positioned onto the isocenter accurately regardless of the position and attitude of the X-ray head. The pan and tilt rotation also provide a small beam's-eye view (BEV) positional deflection around the isocenter without any significant change in the dose distribution. This feature provides an accurate, quick, and easy setup error correction without any couch movement.

In the dynamic treatment mode, the pan and tilt rotations provide a quick pursuit beam motion around the isocenter for the organ motion compensation. Respiratory motion causes the largest motion of a target in the body. The maximum excursion of the target could be as large as ±20 mm in the BEV with a frequency of about 0.3 Hz (19, 25) in and near the lung. A small-angle

rotation (±1.19°) can provide the corresponding motion of the treatment beam around the isocenter with a distance of 96 cm between the isocenter and the gimbals axes. If the X-ray head and gimbals are designed in a mass-balanced manner, and if the inertia around the pan and tilt axes is designed to be small, the X-ray head can be driven to follow the respiratory motion of the target, and it is feasible to compensate for respiratory motion.

Design—overall structure

The overall structure of the system is presented in Fig. 2. The O-ring is structurally rigid. There is no cantilever structure as in a conventional LINAC. The X-ray head is supported by a rigid Rahmen structure, and mechanical distortion is small. A small residual mechanical distortion is compensated for actively by the pan and tilt rotations to an accuracy of less than ±0.1 mm both at the isocenter and at any point within the ±40 mm × ±40 mm BEV area around the isocenter. The skew angle is limited to roughly ±60° by mechanical interference between the couch and the O-ring.

Design—gimbaled X-ray head

The detailed design of the gimbaled X-ray head is shown in Fig. 3. The total height of the X-ray head is 100 cm and the weight is about 600 kg. The X-ray head is driven to rotate around the pan and tilt axes of the gimbals with a pan servo and tilt servo, respectively. The pan and tilt axes are situated at the center of gravity of the X-ray head. The weight, inertia, and rigidity of the gimbaled X-ray head and the rigidity of the O-ring are designed to have a mechanical natural frequency as high as 22 Hz. The pan servo and tilt servo are designed to have the dynamic response of the beam motion of about 2 Hz, for a double amplitude of 8 mm to the command position at the isocenter, with an optimized feed-back and feed-forward controller.

A small and light (35 cm in length and about 10 kg in weight) C-band accelerator guide was newly developed to produce a 6 MV 500 cGy/min (max) photon beam flattened over the 14 cm × 14 cm maximum treatment field. The source axis distance is 100 cm. The multileaf collimator (MLC) design is of the single focus type and has 30 pairs of leaves of 5 mm thickness at the isocenter with

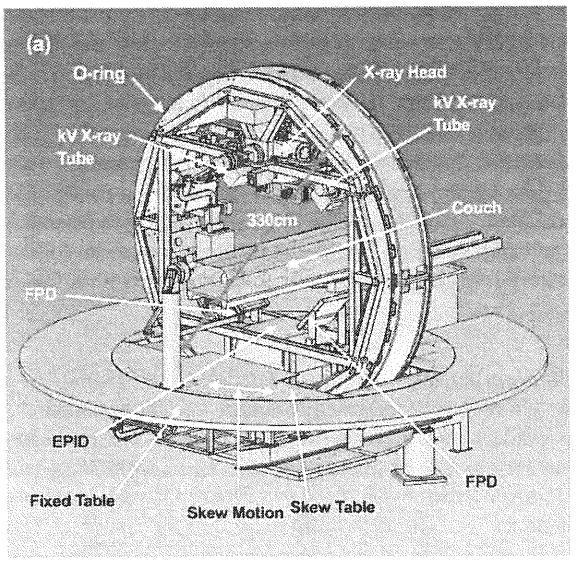

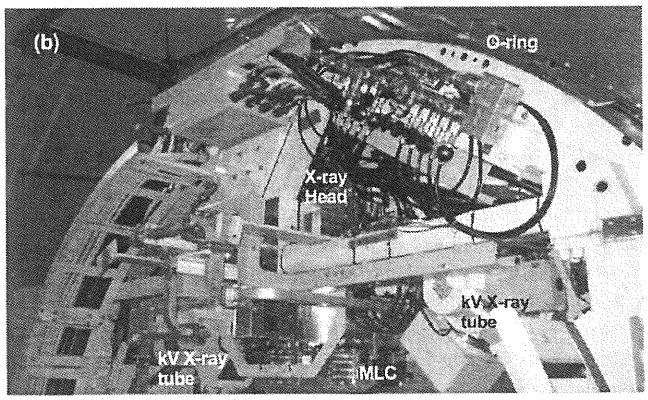

Fig. 2. (a) The basic structure is the O-ring with diameter of about 330 cm. (b) The structure around the X-ray head is shown. The X-ray head is hidden behind the support structure and only the multileaf collimator (MLC) can be seen. The kV X-ray tubes are installed on the both sides of the MLC.

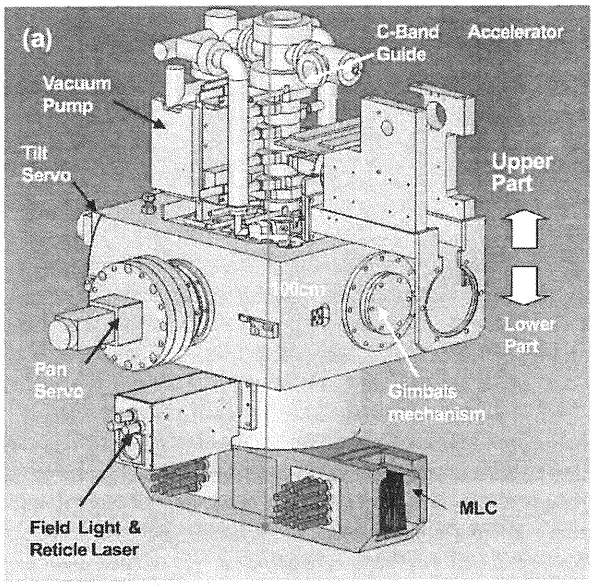

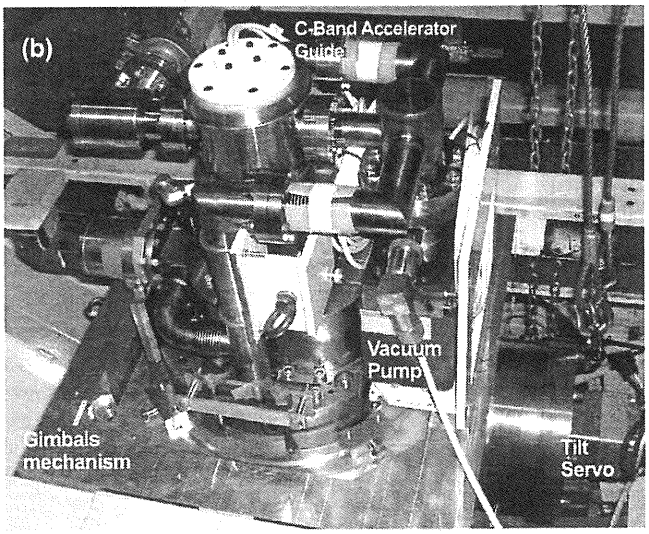

Fig. 3. (a) The gimbaled X-ray head is mainly composed of a C-band accelerator guide, multileaf collimator, and gimbals mechanism. The center of gravity is designed to be at the gimbals axes and the inertia around the gimbals axes is minimized. (b) The upper part of the gimbaled X-ray head is shown. The C-band accelerator guide is situated on the gimbals mechanism.

a field size of 15 cm × 15 cm. The MLC is designed to allow full interdigitation for intensity modulation radiotherapy.

Design—on-board imaging subsystem

Two sets of kV X-ray tubes and FPDs are mounted on the O-ring as the on-board imaging subsystem. (See Figs. 1 and 2.) The stereoscopic imaging subsystem is preferable over a monoscopic imaging subsystem for robust target tracking as pointed out by Berbeco *et al.* (7). The X-ray tube has an operational voltage from 70 kVp to 120 kVp and its heat capacity is 1.5 mega heat units. The FPD has an aperture of 40 cm × 30 cm. The spatial resolution is 1,024 × 768 pixels and the density resolution is 14 bits. The lines of sight are orthogonal to each other. The distance between the kV X-ray source and the isocenter is 100 cm and the distance between the source and the FPD is 188 cm. These values are selected to attain as large a skew angle as possible given the practical limits to the O-ring diameter and the need to use the system for brain applications. The resultant field of view at the isocenter is 21 cm (in the O-ring plane) × 16 cm (perpendicular to the O-ring plane).

For the initial setup and the setup correction, the on-board imaging subsystem is designed to provide 3D information around the target. The operator can determine the X (left-right), Y (craniocaudal), and Z (anteroposterior) setup corrections from two radiographs with proper landmarks. These two radiographs can be compared with prior digitally reconstructed radiographs so that a sixfold (X, Y, Z, roll, pitch, and yaw) setup correction can be made using an image-matching technique.

For the organ motion compensation, the on-board imaging subsystem is designed to provide fluoroscopic views of the target itself or internal fiducial markers on a pair of lines of site to acquire real-time 3D position information about the target. In addition to these radiographic and fluoroscopic imaging capabilities, the on-board imaging subsystem can gather CBCT data with O-ring rotation. Because the O-ring rotation speed is limited to 7°/s by the regulation, it takes 29 s for a single set of an X-ray tube and FPD to gather the CBCT data by rotating 200°. If the two orthogonally mounted X-ray tubes and FPDs are used to gather the CBCT data, it takes 16 s to acquire the data, and the breath-hold method may be acceptable. The reconstruction algorithm is the Feldkamp method and the filtering is with an original function. An antiscatter grid is not provided.

Mechanization—image-guided setup

The couch provides 3D positional correction and the couch motion is expected to be used for a coarse alignment of the planned patient's isocenter with the machine isocenter. After the coarse setup, there is no couch motion for the setup error correction throughout the fraction, which excludes any inaccuracy caused by couch motion. The on-board imaging subsystem is activated to estimate the setup error for the correction. A pair of radiographs is acquired and compared with prior digitally reconstructed radiographs. Landmark comparison or image matching is applied to evaluate the X, Y, and Z positional setup error and the roll, pitch, and yaw rotational setup error (in the case of image matching). The positional setup error is corrected in the BEV plane with the pan and tilt rotation of the X-ray head. Roll and yaw corrections are provided by O-ring rotation and by O-ring skew, respectively. The pitch rotational correction is not available, because neither the couch nor O-ring has a pitch motion capability. The intrafractional patient motion can be compensated for in the same manner without any couch motion. The on-board imaging subsystem is used to monitor the patient motion in the fraction. If the CBCT is available for the setup error evaluation, the lesion could be directly observed and the setup error evaluation would be more reliable.

Mechanization—organ motion compensation

The system uses a pair of views from the on-board imaging subsystem to locate the target. The system operates in two phases. One is the phase for the image acquisition and the other is for the irradiation. In the beginning of the image acquisition phase, the kV X-ray tubes are turned on one at a time and the FPDs accumulate and transfer the charge. The treatment beam is off in the image acquisition phase to avoid the masking effect of the strong scattered radiation of the treatment beam. Because the image acquisition phase lasts for 33 ms, the frequency of the image acquisition phase determines the time allocated for the irradiation phase. During the irradiation phase, the treatment beam is turned on and the FPDs are masked.

The acquired fluoroscopic images are binary-quantized with an optimized threshold to delineate the target, and the center of gravity of the delineated area is tracked as the target centroid. The system calculates the 3D position of the target with a pair of fluoroscopic images.

As presented in Shirato's work (27, 28) on the organ motion in the chest area, the power frequency spectrum analysis of the organ motion shows two major components at 0.3 Hz (low-frequency component) and 1.05 Hz (high-frequency component). The low-frequency component is a respiratory cycle with a maximum amplitude of 25 mm. The high-frequency component is a cardiac cycle observed in the heart abutting area with an amplitude of 1–4 mm. If the system has a mechanical frequency response of more than 0.6 Hz for large amplitudes (±13 mm) and more than 1.5 Hz for small amplitudes (±2 mm), the treatment beam can follow the respiratory motion and even the cardiac motion with a favorable margin.

Preliminary system evaluation

In addition to the basic performance of the treatment X-ray beam, the key performances evaluated were the static beam positioning accuracy, the dynamic response and positioning accuracy for pursuit irradiation, and the capability of the on-board imaging subsystem.

Static beam positioning accuracy

The static positioning accuracy of the treatment X-ray beam, including both the mechanical aiming accuracy and the MLC accuracy, was measured with the on-board EPID. An iron ball of 3/8 inch (9.56 mm) diameter was positioned at the machine isocenter with the center of the iron ball aligned to the machine isocenter. The MLC was set to 3 cm × 3 cm with the center of the field at the isocenter, and 6-MV photons were delivered. The distance between the center of the photon field and the center of the iron ball was defined as the X-ray beam position error from the isocenter. Because the spatial resolution of EPID was 0.2 mm at the isocenter and the measurement included a rather indirect process of determining the center of the X-ray field, the mechanical alignment accuracy was also measured with a charge-coupled device (CCD) camera. The CCD camera was installed at the exit of the MLC and the same iron ball was observed. With this measurement, 1 pixel of the CCD camera corresponded to 0.037 mm at the isocenter.

Dynamic beam response and positioning accuracy

The dynamic beam response and accuracy were measured with the rotary encoder output of the pan servo. The rotary encoder is mechanically coupled to the pan axis and the output of the rotary encoder shows the pan angle position directly. The output of the rotary encoder was compared with the command input of the pan angle. The difference between these values includes both the mechanical error and the mechanical delay, and this difference is the dynamic beam positioning accuracy when the observation of the target position is perfect without any delay or error. The tilt axis has a better dynamic beam response by design and the pan characteristics determine the total dynamic characteristics of the gimbaled X-ray head. The dynamic response was measured with a 0.75 Hz, 20-mm sinusoidal command input as the low-frequency component and a 2.0 Hz, 4-mm sinusoidal command input as the high-frequency component. For the low-frequency component, the maximum beam velocity was 94 mm/s and the maximum beam acceleration was 444 mm/s^2. For the high-frequency component, the maximum beam velocity was 50 mm/s and the maximum beam acceleration was 632 mm/s^2.

Capability of the on-board imaging subsystem

Preliminary studies on the imaging capability were conducted for the CBCT mode and the fluoroscopic mode with real patients. Before the evaluation with real patients, the additional dose from the imaging subsystem was evaluated as shown in Fig. 4 with a PTW CTDI phantom (PTW; Freiburg GMBH, Freiburg, Germany). All patients provided informed consent, and all images of these patients were obtained with the approval of the ethics committee at the Institute of Biomedical Research and Innovation.

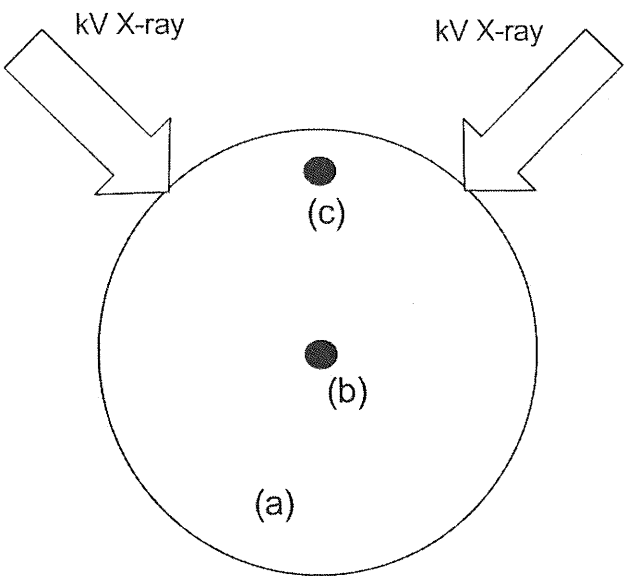

Fig. 4. The phantom configuration used for evaluation of the monitoring dose. (a) CTDI phantom with 320-mm diameter. The ionization chamber of PTW type 30009 was placed for the cone beam computed tomography case (b) and for the fluoroscopy case (c) at the buildup point under the surface where the highest monitoring dose was observed when a pair of shots is provided.

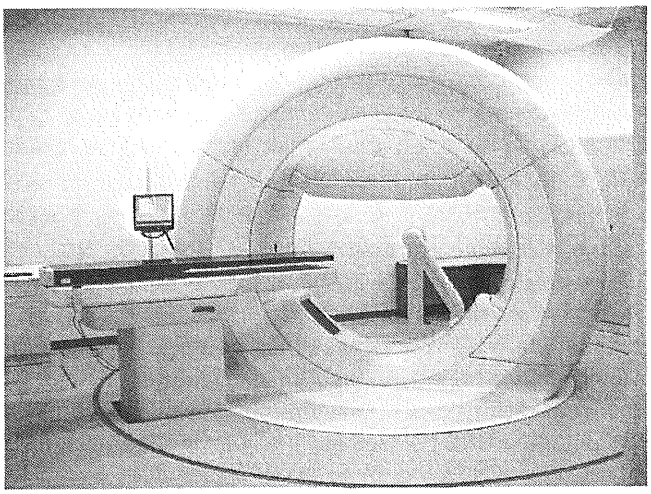

Fig. 5. Exterior view of the system. The O-ring is skewed in the counterclockwise direction.

RESULTS

System exterior view

An exterior view of the system is shown in Fig. 5. The whole system can be housed in the space of a conventional LINAC bunker with appropriate engineering modifications to the floor.

Static beam positioning accuracy

The static positioning accuracy measured for the treatment X-ray beam is shown in Fig. 6. The rms accuracy over the 360° O-ring rotation was 0.08 mm for the pan axis and 0.10 mm for the tilt axis.

The measurement with CCD camera showed a maximum error of 2 pixels, and this corresponded to 0.074 mm as the maximum mechanical error at the isocenter.

Dynamic beam response and positioning accuracy

The dynamic beam response and positioning accuracy are shown in Fig. 7. The mechanical system followed the 0.75 Hz, 20-mm sinusoidal position command with an error and

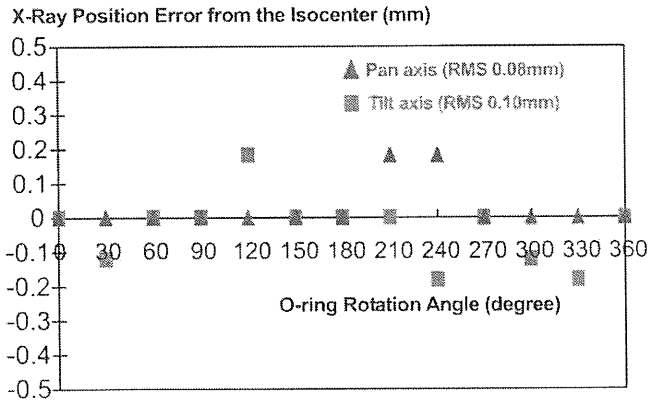

Fig. 6. Static beam positioning accuracy for O-ring rotation was measured with the electronic portal imaging device.

delay of less than 0.6 mm. The mechanical system also followed the 2.0 Hz, 4-mm sinusoidal position command with an error and delay of less than 0.4 mm. The system met our design criteria for positioning the treatment beam on the target both for respiratory organ motion and for cardiac organ motion.

On-board imaging subsystem

A sample of a CBCT image of the pelvis is shown for a prostate case in Fig. 8. The X-ray parameters for the image acquisition were 120 kVp, 200 mA, 10 ms, and 800 mAs. The additional dose from the imaging subsystem was 19.4 mGy. The soft tissues, including the prostate, were identifiable in the CBCT image as clearly as in the conventional X-ray CT. This result was encouraging for the feasibility of the CBCT-based setup.

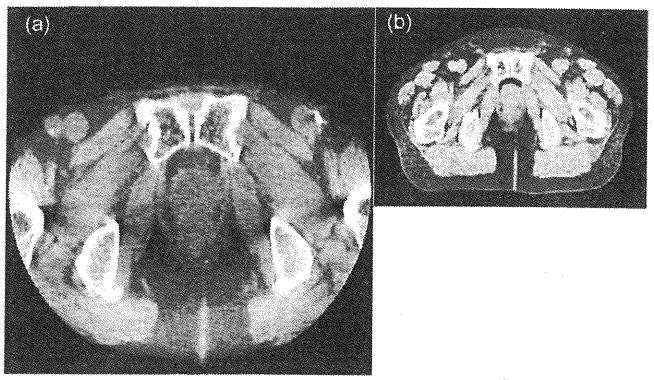

Fig. 8. (a) Cone beam computed tomography image of the pelvis for a prostate case. The X-ray parameters were 120 kVp, 200 mA, 10 ms, and 800 mAs. The total monitoring dose was 19.4 mGy. (b) The conventional X-ray computed tomography image of the same area of the same patient.

An image of the lung in the fluoroscopic mode is shown in Fig. 9. The X-ray parameters were 110 kVp, 80 mA, and 5 ms per shot. The additional dose from the imaging subsystem was 0.117 mGy per pair of stereo shots. The image quality was good enough to discern the tumor itself from the background for automatic detection and tracking with binary quantization.

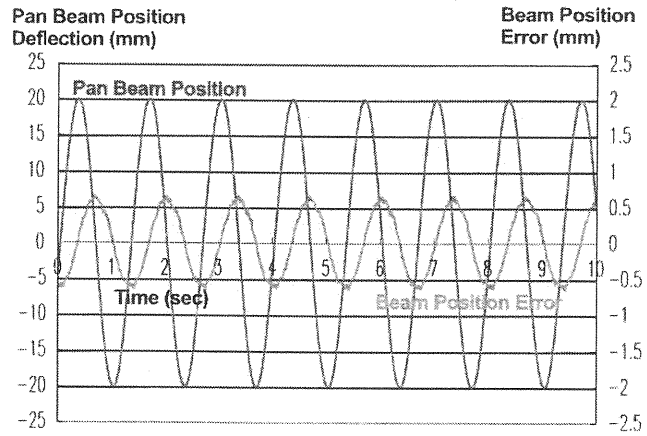

Fig. 7. (a) Low-frequency dynamic response and accuracy were measured with the pan servo commanded by a sinusoidal input of 0.75 Hz, 20 mm. The blue line shows the pan beam position measured with the rotary encoder output and the red line is the difference between the command value and the rotary encoder output. (b) High-frequency dynamic response and accuracy were measured with the pan servo commanded with a sinusoidal input of 2.0 Hz, 4.0 mm. The blue line shows the pan beam position measured with the rotary encoder output and the red line is the difference between the command value and the rotary encoder output.

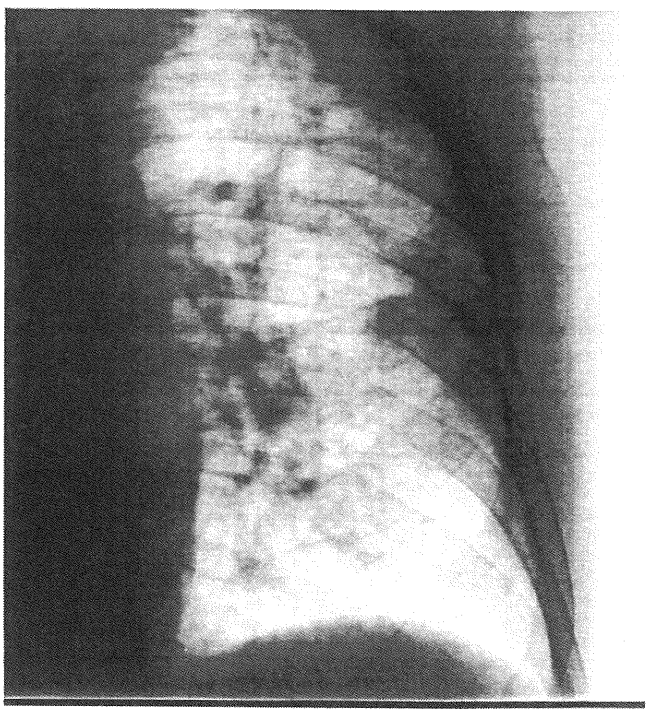

Fig. 9. Fluoroscopic lung image. The X-ray parameters were 110 kVp, 80 mA, and 5 ms per shot. The monitoring dose was 0.117 mGy per pair of stereo shots.

DISCUSSION

We have introduced the concept of a 4D-IGRT system with gimbaled X-ray head. The innovative gimbals mechanism enables both a precise setup and a quick beam motion suitable for compensation of respiratory and cardiac organ motion. The static positional error and the dynamic response of the treatment X-ray beam met our design criteria. In the CBCT mode, the prostate was clearly identifiable. The CBCT performance was encouraging for the practical feasibility of CBCT-based setup. The fluoroscope performance for the lung showed the feasibility of tracking the tumor itself without the use of surrogate internal fiducial markers.

CBCT-based setup

The CBCT has a far better space and density resolution than the radiograph and is thought to provide better information for setup error correction. In many cases, CBCT will give direct images of the tumor itself. Radiographs mostly give only anatomic information around the tumor except in the lung area. The tumor position should be estimated from visible landmarks or markers, or it should be determined by image matching using prior digitally reconstructed radiographs. We think that the future trend of IGRT will be toward on-board CBCT imaging. The setup error measurement will be carried out with direct tumor images from the on-board CBCT and preacquired multimodality fused images with the patient in the treatment position on the couch.

Target tracking

In the organ motion compensation mode, target tracking is critical. Although the mechanical system can follow the organ motion, any real-time imaging system inevitably has some amount of delay for image acquisition and image processing. For example, the low-frequency component of the respiratory motion has a 24.5 mm/s maximum velocity for a 13-mm amplitude, 0.3 Hz sinusoidal motion. The delay of the on-board imaging subsystem is 66 ms (33 ms for image acquisition and another 33 ms for image processing and position calculation) with our system. This delay causes a maximum positional error of 1.6 mm. This delay is the reason why the mechanical system should not be directed to the observed position but to the estimated position, which takes account at least of the delay of the imaging subsystem, to get a favorable target tracking accuracy. An accurate mathematical model of the target motion is important for accurate estimation. The present target motion model is a rather simple one determined from the averaging of several respiratory cycles. A finite state model like that proposed by Wu *et al.* (29) would be one promising option for the improvement of our system.

The stability and reliability of the target tracking are also important. Target tracking by the on-board imaging subsystems should continue stably during the irradiation period. Our present scheme of target tracking is to track the real image of the tumor in the lung area with fluoroscopy. However, the stability and the reliability of this tracking mode are not sufficient and are affected by blockage due to the surrounding high-density bones or organs. High X-ray contrast internal fiducial markers may improve stability and reliability at the cost of rather invasive marker installation performed percutaneously or with bronchofibroscopy. In areas other than the lung, internal fiducial markers will be mandatory for the fluoroscopy mode. The merits and demerits of internal fiducial markers require rigorous clinical study.

Future work

The system is still in an early phase of evaluation. We are evaluating the basic functions and performance. After rigorous evaluation with static and moving phantoms, we are planning a series of clinical evaluations starting with the static treatment mode. For the dynamic treatment mode, the treatment planning solution will be the key issue, in addition to stable and reliable target tracking with an acceptable amount of additional dose from the imaging subsystem. The appropriate imaging dose is another important issue. Our research is still in a preliminary stage and this issue should be investigated rigorously, including the methods for the measurement of the imaging dose. We are starting rigorous research on these clinical and technical areas.

The deformation of the PTV can be compensated with the leaf motion of the MLC combined with the organ motion compensation with the pan and tilt dynamic beam motion. But it seems better to include the deformation in the margin presently, because real-time tracking of the deformation will be clinically difficult and further study is needed to improve this technique.

CONCLUSIONS

Key functions and capabilities of our new system are very promising for precise image-guided setup and for tracking and pursuit irradiation of a moving target.

REFERENCES

1. Meertens H, van Herk M, Bijhold J, *et al.* First clinical experience with a newly developed electronic portal imaging device. *Int J Radiat Oncol Biol Phys* 1990;18:1173–1181.
2. Adler JR Jr., Chang SD, Murphy MJ, *et al.* The Cyberknife: A frameless robotic system for radiosurgery. *Stereotact Funct Neurosurg* 1997;69:124–128.
3. Weiss E, Vorwerk H, Richter S, *et al.* Interfractional and intrafractional accuracy during radiotherapy of gynecologic carcinomas: a comprehensive evaluation using the ExacTrac system. *Int J Radiat Oncol Biol Phys* 2003;56:69–79.
4. Jaffray DA, Drake DG, Moreau M, *et al.* A radiographic and tomographic imaging system integrated into a medical linear accelerator for localization of bone and soft-tissue targets. *Int J Radiat Oncol Biol Phys* 1999;45:773–789.
5. Uematsu M, Shioda A, Tahara K, *et al.* Focal, high dose, and fractionated modified stereotactic radiation therapy for lung

carcinoma patients: A preliminary experience. *Cancer* 1998; 82:1062–1070.
6. Jaffray DA, Siewerdsen JH, Wong JW, *et al.* Flat-panel cone-beam computed tomography for image-guided radiation therapy. *Int J Radiat Oncol Biol Phys* 2002;53:1337–1349.
7. Berbeco RI, Jiang SB, Sharp GC, *et al.* Integrated radiotherapy imaging system (IRIS): Design considerations of tumour tracking with linac gantry-mounted diagnostic x-ray systems with flat-panel detectors. *Phys Med Biol* 2004;49: 243–255.
8. Smitsmans MH, de Bois J, Sonke JJ, *et al.* Automatic prostate localization on cone-beam CT scans for high-precision image-guided radiotherapy. *Int J Radiat Oncol Biol Phys* 2005;63: 975–984.
9. Nakagawa K, Aoki Y, Tago M, *et al.* Megavoltage CT-assisted stereotactic radiosurgery for thoracic tumors: Original research in the treatment of thoracic neoplasms. *Int J Radiat Oncol Biol Phys* 2000;48:449–457.
10. Sidhu K, Ford EC, Spirou S, *et al.* Optimization of conformal thoracic radiotherapy using cone-beam CT imaging for treatment verification. *Int J Radiat Oncol Biol Phys* 2003;55:757–767.
11. Ruchala KJ, Olivera GH, Schloesser EA, *et al.* Megavoltage CT on a tomotherapy system. *Phys Med Biol* 1999;44:2597–2621.
12. Shimizu S, Shirato H, Kitamura K, *et al.* Use of an implanted marker and real-time tracking of the marker for the positioning of prostate and bladder cancers. *Int J Radiat Oncol Biol Phys* 2000;48:1591–1597.
13. Keall P. 4-dimensional computed tomography imaging and treatment planning. *Semin Radiat Oncol* 2004;14:81–90.
14. Neicu T, Berbeco R, Wolfgang J, *et al.* Synchronized moving aperture radiation therapy (SMART): Improvement of breathing pattern reproducibility using respiratory coaching. *Phys Med Biol* 2006;51:617–636.
15. Schweikard A, Glosser G, Bodduluri M, *et al.* Robotic motion compensation for respiratory movement during radiosurgery. *Comput Aided Surg* 2000;5:263–277.
16. Schweikard A, Shiomi H, Adler J. Respiration tracking in radiosurgery. *Med Phys* 2004;31:2738–2741.
17. Keall PJ, Todor AD, Vedam SS, *et al.* On the use of EPID-based implanted marker tracking for 4D radiotherapy. *Med Phys* 2004;31:3492–3499.
18. Berson AM, Emery R, Rodriguez L, *et al.* Clinical experience using respiratory gated radiation therapy: Comparison of free-breathing and breath-hold techniques. *Int J Radiat Oncol Biol Phys* 2004;60:419–426.
19. Harada T, Shirato H, Ogura S, *et al.* Real-time tumor-tracking radiation therapy for lung carcinoma by the aid of insertion of a gold marker using bronchofibroscopy. *Cancer* 2002;95: 1720–1727.
20. Shirato H, Shimizu S, Kunieda T, *et al.* Physical aspects of a real-time tumor-tracking system for gated radiotherapy. *Int J Radiat Oncol Biol Phys* 2000;48:1187–1195.
21. Zhang T, Keller H, O'Brien MJ, *et al.* Application of the spirometer in respiratory gated radiotherapy. *Med Phys* 2003; 30:3165–3171.
22. Murphy MJ. Tracking moving organs in real time. *Semin Radiat Oncol* 2004;14:91–100.
23. Keall PJ, Joshi S, Vedam SS, *et al.* Four-dimensional radiotherapy planning for DMLC-based respiratory motion tracking. *Med Phys* 2005;32:942–951.
24. Papiez L, Rangaraj D, Keall P. Real-time DMLC IMRT delivery for mobile and deforming targets. *Med Phys* 2005; 32:3037–3048.
25. Suh Y, Yi B, Ahn S, *et al.* Aperture maneuver with compelled breath (AMC) for moving tumors: A feasibility study with a moving phantom. *Med Phys* 2004;31:760–766.
26. Webb S. Limitations of a simple technique for movement compensation via movement-modified fluence profiles. *Phys Med Biol* 2005;50:N155–N161.
27. Shirato H, Seppenwoolde Y, Kitamura K, *et al.* Intrafractional tumor motion: Lung and liver. *Semin Radiat Oncol* 2004;14: 10–18.
28. Seppenwoolde Y, Shirato H, Kitamura K, *et al.* Precise and real-time measurement of 3D tumor motion in lung due to breathing and heartbeat, measured during radiotherapy. *Int J Radiat Oncol Biol Phys* 2002;53:822–834.
29. Wu H, Sharp GC, Salzberg B, *et al.* A finite state model for respiratory motion analysis in image guided radiation therapy. *Phys Med Biol* 2004;49:5357–5372.

Small Cell Lung Carcinoma: Eight Types of Extension and Spread on Computed Tomography

Nobukata Kazawa, MD, Masanori Kitaichi, MD, PhD,† Masahiro Hiraoka, MD, PhD,* Kaori Togashi, MD, PhD,* Naoshi Mio, MD, PhD,‡ Michiaki Mishima, MD, PhD,‡ and Hiromi Wada, MD§*

Objective: The aim of this study was to classify the types of tumor extension and spread of small cell lung carcinoma (SCLC) and to recognize the unusual types of spread pattern of SCLC on computed tomography (CT) including multidetector row CT (MDCT) using contrast-enhanced material.

Materials and Methods: Sixty-eight cases (53 men and 15 women aged 54–83 years old) of pathologically proven SCLC were examined mainly by contrast-enhanced CT scan. In surgically treated 7 cases, CT-pathologic correlations were performed.

Results: Eight types of extension and spread were recognized by the examinations of chest CT. The type of central mass + mediastinal extension (n = 20 [29.4%]) was the most common manifestation. The types of central perihilar mass (n = 12 [17.6%]), peripheral mass + mediastinal extension (n = 14 [20.6%]), and peripheral mass (n = 7 [10.3%]) were frequently observed. The primary site of SCLC was in peripheral lung tissue in 21 of 68 cases (30.9%) in this study. Unusual CT manifestations, such as the types of lymphangitic spread (n = 6 [8.8%]), pleural dissemination (n = 4 [5.9%]), lobar replacement (n = 3 [4.4%]), pneumonialike air-space infiltrative spread (n = 2 [2.9%]) were recognized in our study. Stenosis of trachea and main bronchus caused by peribronchial extension were commonly noted. In the advanced cases with mediastinal extension, we observed the extension of SCLC to superior vena cava (n = 22), main pulmonary artery (n = 18), pulmonary vein (n = 11), and thoracic aortic wall (n = 7). Peri-and intracardial invasions were also observed in 9 cases.

Conclusions: Computed tomography including MDCT analysis revealed 8 types of extension and spread of SCLC including unusual forms in 68 SCLC cases. Peribronchial extension and great vessel wall involvement, such as superior vena cava, main pulmonary artery, and peri-/intra-cardial extension, were commonly observed in advanced stage.

Key Words: small cell carcinoma, lymphangitic spread, pleural dissemination, lobar replaced extension, air-space consolidation, peri-bronchial extension, great vessel wall involvement, peri/intracardial extension

(*J Comput Assist Tomogr* 2006;30:653–661)

From the *Departments of Radiology, †Anatomic Pathology, ‡Respiratory Medicine, and §Thoracic Surgery, Kyoto University Hospital, Shogoin Kawaharamachi 54 Sakyo, Kyoto-City, Kyoto Prefecture Japan.

Received for publication January 22, 2006; accepted March 1, 2006.

Reprints: Nobukata Kazawa, Departments of Radiology, Kyoto University Hospital, Shogoin Kawaharamachi 54 Sakyo, Kyoto-City, Kyoto Prefecture 606-8507 Japan (e-mail: nk1207@kuhp.kyoto-u.ac.jp).

Among lung malignant neoplasm including bronchogenic lung carcinoma, small cell lung carcinoma (SCLC) is prognostically the worst one which usually grows very rapidly, and disseminates even at the first visit to a hospital. Its doubling time was estimated to be about 30–60 days.[1–5] However, therapeutic results of radiotherapy and chemotherapy using new agents, such as irinotecan (CPT-11) or pacritaxel combined with cisplatin, have been improving.[6–8] Therefore, early detection and the correct diagnosis of SCLC are very important. However, there is scant information of the CT and contrast-enhanced CT imaging features of SCLC in the literature.[1,6,9] The classification of limited or extensive disease of SCLC is routinely used when choosing the therapeutic options.[10–12] For systematic analysis of the tumor extension and spread, we retrospectively reviewed the CT images and clinical data of 68 SCLC cases with special interest of invasion to airway and great vessels wall. In some cases, life-threatening tumor invasion to the peri-/intracardium or aortic artery was observed. Unusual types, such as lymphangitic spread, pleural dissemination, lobar replacement, and air-space consolidation, were recognized in our study. To the best of our knowledge, this is the first study describing clearly these 4 atypical types of extension and spread of SCLC.

MATERIALS AND METHODS

The extension and spreading patterns were evaluated with chest CT mainly by contrast-enhancement method (CE-CT). Brain, abdominal, and neck-chest screening CT scan, and/or brain MRI were also performed routinely to detect distant metastasis. The CT images and clinical and laboratory data of consecutive 68 patients with SCLC (53 men, 15 women; 54–83 years old; mean age, 65.4 years old) were examined from July 1998 to June 2004 in Kyoto University Hospital. Among them, 23 cases had limited disease (LD) in whom carcinoma was confined to one hemithorax, mediastinum, and ipsilateral supraclavicular lymph nodes.[1,10,11] The other 45 cases had extended disease (ED) in whom carcinoma had spread beyond LD. We used 2 helical CT (Hi-Speed Advantage GE medical system Milwaukee, Wis and X-Vigor Toshiba Tokyo) and multidetector row CT (MDCT) scanner (Aquillion Toshiba Tokyo) with 3–7-mm slice thickness. In the 21 cases of SCLC, chronic interstitial pneumonitis was also recognized. High-resolution CT (2-mm collimation section using high-spatial-frequency algorithm) scans were also used for the evaluation of severity and the follow-up observation of the chronic interstitial pneumonia. In 63 of 68 patients, CE-CT images were obtained with intravenous

TABLE 1. CT findings in 68 Patients of Small Cell Lung Carcinoma

Type of Extension and Spread	Airway Stenosis			Invasion of Great Vessel Wall				Peri-or Intracardial Invasion		Pleural Effusion	Pericardial Effusion	Distant Metastasis at Presentation (Number of Organs)
(n =) number of patients	SS	LS	TM	SVC	main PA	main PV	Aorta	Peri-	Intra-			
Central peri-hilar type (n = 12)	7	6	7	2	3	(–)	(–)	(–)	(–)	8	2	
Central + mediastinal extension type (n = 20)	4	7	14	12	9	4	4	2	2	5	6	N = 9; Br 2 Li4 Ad1 Bo2 LN2 contL3 Pan2 Sc 1
Peripheral type (n = 7)	(–)	(–)	(–)	(–)	(–)	(–)		(–)		(–)	(–)	
Peripheral + mediastinal extension type (n = 14)	2	2	5	4	3	3	2	3	0	6	4	N = 5; Br2 Li3 Ad3 Bo3 LN2 Pr1 Orp1
Lymphangitic spread type (n = 6)	3	4	5	2	2	3	1	3	0	6	2	N = 4; Br2 Li2 Ad1 Bo1 LN3 Spc 1
Pleural dissemination type (n = 4)	(–)	(–)				(–)	(–)	(–)	(–)	4	(–)	
Lobar replacement type (n = 3)	3	3	3	2	1	1	(–)	(–)	(–)	1	(–)	N = 2; Br1 Li2 Ad1 Bo1 LN1
Air-space onsolidation type (n = 2)	1	(–)	(–)	(–)	(–)	(–)	(–)	(–)	(–)	1	(–)	N = 1; Li1
Total (n = 68)	20	23	34	22	18	11	7	8	2	31	14	N = 21; Br7 Li12 Ad6 Bo7 LN8 contL3 Pan2 Pr1 Sc 1 Orp1 Spc 1

SS indicates subsegmental bronchus level; LS, lobar-segmental bronchus level; TM, trachea-main bronchus; SVC, superior vena cava; PA, pulmonary artery; PV, pulmonary vein; Br, brain; Li, liver; Ad, adrenal gland; Bo, bone; LN, abdominal or neck lymph node; cont L, contralateral Lung; Pan, pancreas; Sc, subcutaneous; Pr, prostate; Orp, oropharynx; Spc, spinal cord.

administration of 100–150 mL of iodinated, nonionic contrast material. Computed tomography scans were reviewed retrospectively by at least 2 experienced radiologists. Images were viewed at both lung (level-600, width 1500) and mediastinal (level 60, width 400) settings. The pathologic diagnosis of SCLC was obtained by cytology (sputum n = 8, pleural effusion n = 9, and transbronchial brushing n = 5), or histology (transbronchial lung biopsy [TBLB]) (n = 22), lymph node biopsy (n = 10), percutaneous mediastinal biopsy (n = 5), percutaneous lung biopsy (n = 2), and/or surgical open lung biopsy (n = 7). Lymph node (LN) metastasis was radiologically estimated to be present when the short-axis diameter of LN was 10 mm or greater.[6,12] Lesions, such as airway stenosis, invasion of great blood vessel wall, intra-or pericardial invasion, pleural effusion, pericardial effusion, and distant metastasis, were evaluated. The anatomic location and

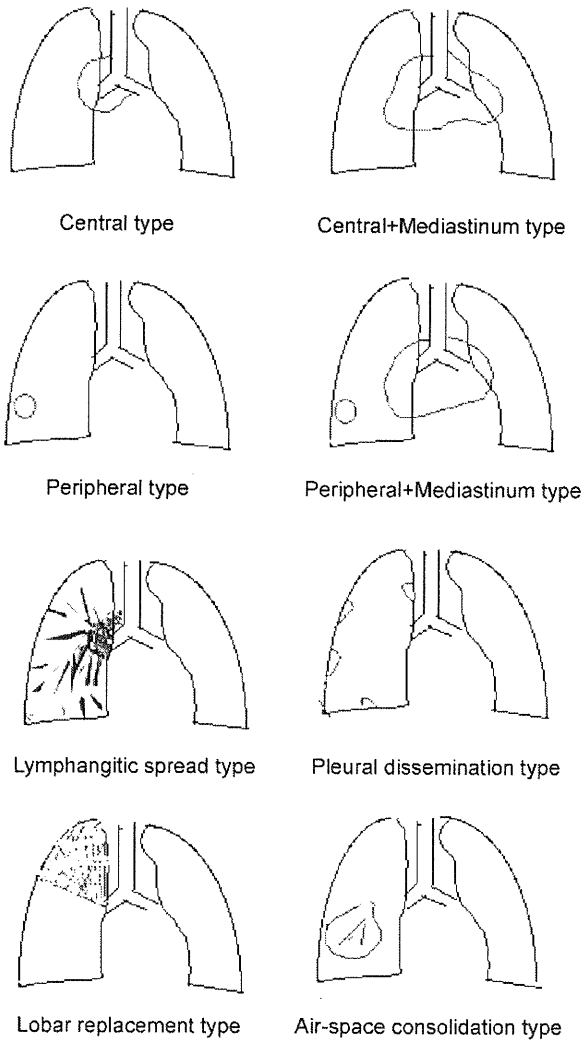

FIGURE 1. The schema of 8 types of the tumor extension and spread pattern of SCLC; central perihilar type, central + mediastinal extension type, peripheral type, peripheral + mediastinal extension type, lymphangitic spread type, pleural dissemination type, lobar replacement type, and air-space consolidation type.

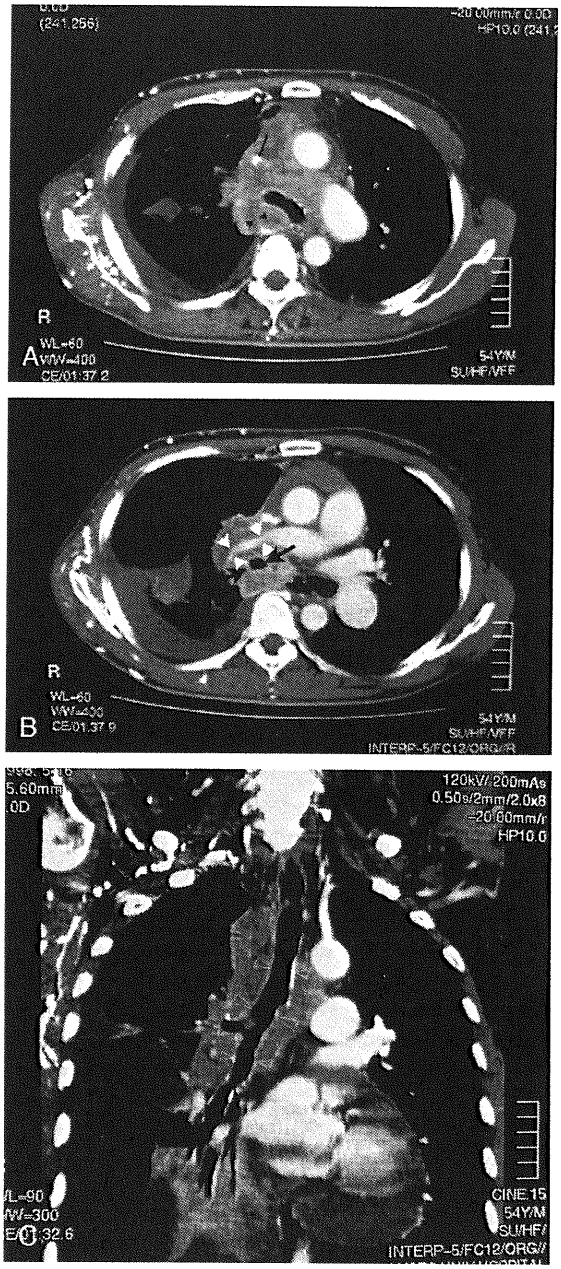

FIGURE 2. Central + mediastinal extension type of SCLC with peribronchial extension. A, A 54-year-old man with diffuse infiltration of heterogeneously enhanced tumor from right hilar area to mediastinum. Severe extrinsic compression (grade 3 stenosis) of SVC (arrows) and azygos vein occlusion (arrowheads) was demonstrated (cT4N3M0 clinical stage IIIB ED). B, The tumor narrowed the lumen of main bronchus moderately (arrows) and the right main PA was severely encased (grade 2 stenosis) (arrowheads). Abnormal dilatation of superficial vein was clearly observed in the ventro-lateral chest wall and around right scapular bone, indicating that they functioned as collateral blood vessels. C, On coronal reconstruction view, its peribronchial submucosal extension was clearly shown with preservation of calcified bronchial wall (open arrowheads). A tiny spherical mass protruding into the lumen of bronchus was also presented. Moderate amount of pleural effusion and small amount of pericardial effusion were also observed.

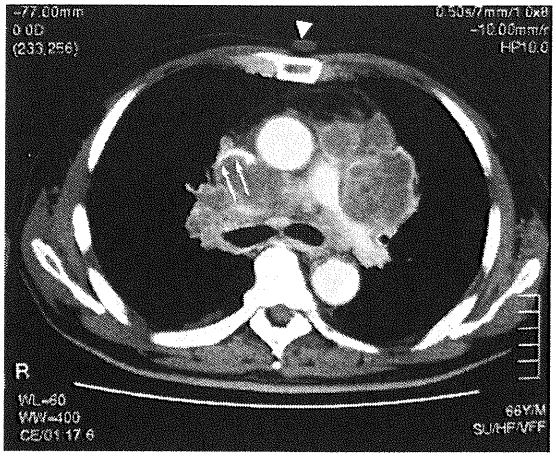

FIGURE 3. Central + mediastinal extension type invading to SVC: A 66-year-old man presented heterogeneously low-dense huge mass lesion conglomerated with lymph node metastases involving bilateral mediastinum. The mass lesion was compressively projecting to the SVC (arrows). The right main PA was compressed and displaced caudally. In the anterior chest wall, skin metastasis which was proved by subcutaneous biopsy was demonstrated as a low-dense nodule (arrowhead) (cT4N3M1 c-stage ED).

distribution of the primary lung tumor and calcification were also assessed. The degree and pattern of tumor and lymph node enhancement were also evaluated. The final assessment of the CT findings was obtained by consensus in each case between the 2 radiologists always including 1 (N.K.). In 7 surgically treated cases of SCLC (6 peripheral type and 1 central perihilar type), we compared the CT features with histologic findings in the resected lung specimens.

Definition of types of local extension and spread of SCLC was as follows: When a central perihilar mass was recognized, we called central perihilar type. Contrast with central type in which carcinoma is confined within ipsilateral mediastinum, we defined central + mediastinal extension type as that extending to contralateral mediastinal tissue. When primary carcinoma was located only in peripheral lung field, we defined it as peripheral type. When combinations of a peripheral tumor and a hilar/ipsilatreal mediastinal lymphadenpathy were recognized, we defined as peripheral + mediastinal extension type. We discriminated between peripheral type and peripheral + mediastinal extension type by the assessment of mediastinal nodal metastasis (N2). The lymphangitic spread type in the lung field was recognized when the irregular thickening of broncho-vascular bundles and prominent interlobular septal lines in the lung fields with pleural effusion were noted.

For the cases with multiple subpleural small nodular shadows associated with malignant pleural effusion, we called pleural dissemination type. In the lobar replacement type, huge mass lesion replacing one lobe entirely was observed on CT. We called air-space consolidation type when poorly marginated consolidation with tubular or cystic air-bronchiologram was recognized in the lung mass lesion on CT imaging. Informed consent was obtained from each patient. This study was approved by our institutional ethics committee.

RESULTS

The Extension and Spread Patterns of SCLC Elucidated by CT Analysis

By the CT imaging, we could classify the tumor spreading patterns (Table 1) of the consecutive 68 SCLC into 8 different types (Fig. 1): namely, central perihilar type (n = 12 [17.6%]), central+ mediastinal extension type (n = 20 [29.4%]) (Figs. 2, 3), peripheral type (n = 7 [10.3%]), peripheral + mediastinal extension type (n = 14 [20.6%]) (Fig. 4), lymphangitic spread type (n = 6 [8.8%]) (Fig. 5), pleural dissemination type (n = 4 [5.9%]), lobar replacement type (n = 3 [4.4%]) (Fig. 6), air-space consolidation type (n = 2 [2.9%]) (Fig. 7).

Among the 8 types, unusual spreading patterns of SCLC were lymphangitic spread type, pleural dissemination type, lobar replacement type, and air-space consolidation type.

The type of lymphangitic tumor spread was assessed to be present in 6 cases when we observed the abnormal thickening of the lung interstitial tissue such as the broncho-vascular bundle and the interlobular septum with pleural effusion (Fig. 5).[14]

In the lobar replacement type as Figure 6, the heterogeneously enhanced mass replacing normal lung parenchyma in entire right upper lobe was observed. It was well demarcated by interlobar and parietal pleural membrane. In another 2 cases of this type, well-demarcated wedge-shaped expanding tumor was demonstrated. In any cases, no apparent chest wall invasion was observed.

In the air-space consolidation type (Fig. 7A–C), we saw indistinct infiltrative opacity with faint air-alveolar or air-bronchiologram was observed. Opacified slightly narrowed pulmonary vessels were well demonstrated at the segmental branch level on contrast-enhanced CT. Although, it is difficult to differentiate from primary lung tumor with obstructive pneumonia at the time of presentation, we regarded this infiltrative shadow reflects the spread of SCLC because the improvement after the intensive chemotherapy was observed.

The Airway Stenosis

The stenosis of trachea and main bronchus (Table 2) caused by peribronchial extension was frequently observed on CT (Fig. 2A–C) (trachea-major bronchial stenosis; n = 34 [50%], stenosis of lobar-segmental branches; n = 23 [33.8%], and stenosis of subsegmental branches; n = 20 [29.4%]). By using coronal reconstructive images derived from MDCT scan such as Figure 2C, its peribronchial submucosal extension was clearly shown with almost preservation of bronchial inner wall. Postobstructive pneumonia and/or bronchiolitis in the peripheral lung field were rarely observed among the study group of SCLC (n = 5 [7.3%]).

The Invasion of Great Vessel Walls

It was observed in many (n = 30 [44.1%]) cases that the vessel walls, such as superior vena cava (SVC) or pulmonary artery (PA), were involved by the tumor and mediastinal adenopathy (SVC: n = 22 [32.3%]), main PA: n = 18 [26.4%], main pulmonary vein (PV): n = 11 [16.1%], thoracic aorta:

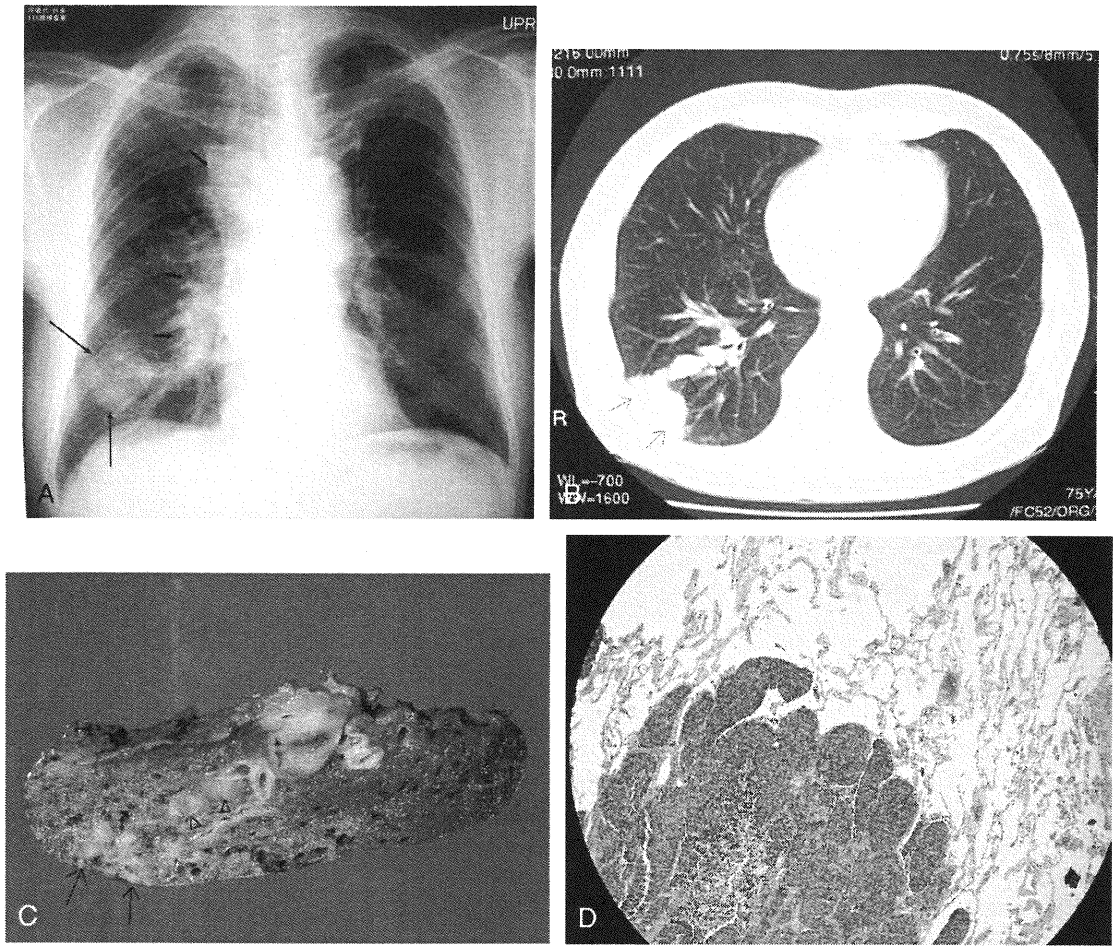

FIGURE 4. Peripheral + mediastinal extension type. A, Posteroanterior chest radiograph of a 75-year-old man showed mass shadow (long arrows) in the right lower lobe. The huge right paratracheal and hilar lymphadenopathy (arrows) were also observed (cT1N2M0 c-stage IIIA LD). B, The preoperative CT scan showed well-demarcated subpleural tumor in the right lower lobe (segment S9-S10 area) (arrows) with daughter small nodules (arrowheads) distributing along the peribronchovascular lung field. Right upper mediastinal and hilar lymphadenopathy were observed. In the lung bases, mild fibrotic interstitial pneumonitis was also observed (not shown). C, The cut surface of resected lung specimen revealed the clearly defined mainly white to tan subpleural mass (arrows) and some peribronchovascular nodules (arrowheads). At the proximal perihilar area, massive lymphadenopathy was also observed. D, Pathologic study of a surgical lung biopsy showed the tumor cell growth with nest formation filling alveolar air spaces with sharp margin (Hematoxylin and Eosin stain ×20).

n = 7 [10.3%]). The grades of tumor invasion to the adjacent great vessel were summarized in Table 2 (grade 1 = mild luminal stenosis with wall irregularity, grade 2 = moderate compressive stenosis caused by tumor encasement, grade 3 = severe constrictive stenosis or luminal invasion). (Tables 1, 2)

These findings were mainly observed in the mediastinal extension type. The involvement of great blood vessel wall was observed in 22 of 34 cases (64.7%) of mediastinal extension type (15 of 20 cases of central + mediastinal extension type, and 7 of 14 cases of peripheral + mediastinal extension type). Among them, apparent invasion of SVC was assessed to be present when it was almost completely obstructed (n = 4) or polypoid luminal-enhanced mass was observed on CE-CT (n = 3) (grade 3 stenosis). We suspected tumor penetration into the adventitia of SVC in cases of grade 2 stenosis (n = 8). In some cases, intravenous thrombosis which was not enhanced by CE-CT was also observed in SVC or brachiocephalic vein. Severe constrictive stenosis to occulusive change of main PA and PV was observed in 11 (Fig. 2B) and 6 cases, respectively. The involvement of the thoracic aortic wall was assessed to be present in 7 cases when the mass lesion abutting on more than 50% of the circumference of aorta or severe irregular deformity of outer wall was observed. Also the azygos vein occlusion and several collateral superficial veins in the chest wall, as in Figure 2A, were observed.

The Distant and Lymph Node Metastasis

The distant metastasis which was confirmed by biopsy or follow-up CT were recognized in: liver (n = 12), brain (n = 7), bone (n = 7), adrenal gland (n = 6), neck lymph-node (n = 4), abdominal lymph node (n = 4), contralateral lung (n = 3), pancreas (n = 2), prostate (n = 1), spinal cord (n = 1), and oropharynx (n = 1). In 8 cases of peripheral + mediastinal extension type,

FIGURE 5. The lymphangitic tumor spread type. The right main bronchus was moderately narrowed by the tumor. The irregular nodular thickening of the bronchovascular bundles (arrowheads) extending from the hila peripherally and prominent interlobular septa (arrows) was observed. Small amount of pleural effusion were accompanied. Subpleural mass surrounded by ground glass opacities was also observed in lung parenchyma (a 68-year-old man c-T4N2M1 c-stage IV ED).

multiple lung nodules which we thought intrapulmonary metastasis were also observed (5 within the same lobe with the primary SCLC, 3 in bilateral lungs). Lymph node metastases were observed in 65 (95.6%) of the 68 cases (Table 1).

Other Findings and Radiologic-Pathologic Correlation

In many subjects, cardiac compressive deformities were observed on CT. The tumor extension into the intra-(n = 2) and pericardium (n = 8) by the CT findings was diagnosed when the tumor extension to the left atrium of the heart or irregular thickening of the pericardium[13] was observed (Table 1).

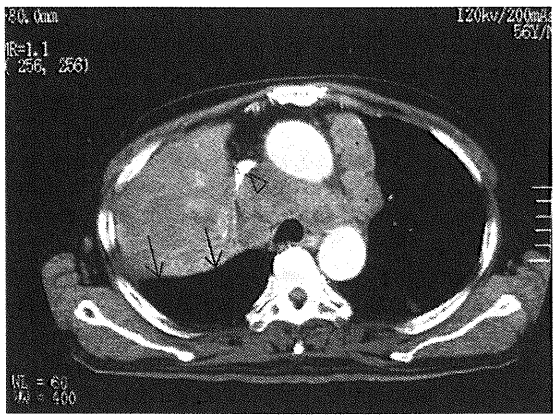

FIGURE 6. The lobar replacement type. Slightly enhanced soft tissue density huge tumor replacing entire right upper lobe was noted. However, the tumor did not invade the major fissure (arrows) nor chest wall. SVC was severely compressed by tumor tissue with central line catheter (arrowheads). Metastatic lymphadenopathy was also noted (asterisks) in contra-lateral left mediastinum (an 81-year-old man c-T2N2M1 c-stage ED).

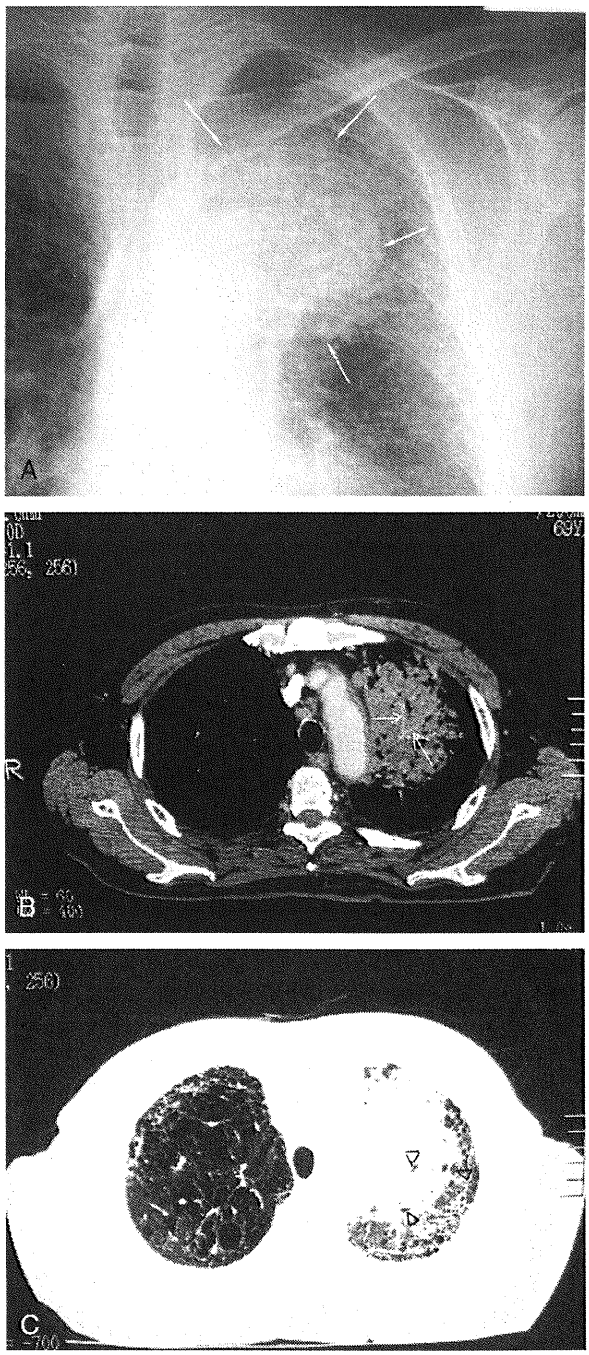

FIGURE 7. The air-space consolidation type. A, Posteroanterior chest radiograph shows pneumonialike infiltrative shadow (arrow) in the left upper lobe. The outer contour of the aortic arch was silhouetted out by the abnormal infiltrative shadow (a 69-year-old man c-T2N2M1c-stage ED). B, Contrast enhanced slightly narrowed pulmonary vessels (arrows) within the area of consolidation were noted on mediastinal window setting. C, 2 mm collimation HRCT image showed poorly marginated air space consolidation with cystic change like air-bronchiologram (arrowheads) on lung window setting. Severe emphysematous change and mild reticulo-nodular shadows representing interstitial pneumonitis were also observed.

TABLE 2. Relationship of Extension and Spread Types of SCLC With Invasion of Great Vessel

	SVC			Main PA			Main PV			Aorta		
N = number of patients	**Grade 1**	**Grade 2**	**Grade 3**	**Grade 1**	**Grade 2**	**Grade 3**	**Grade 1**	**Grade 2**	**Grade 3**	**Grade 1**	**Grade 2**	**Grade 3**
Cental peri-hilar type (n = 12)	1	1	0	1	1	1		(–)			(–)	
Central+ mediastinal extension type (n = 20)	2	5	5	0	2	7	1	1	2	2	2	0
Peripheral type (n = 7)		(–)			(–)			(–)			(–)	
Peripheral + mediastinal extension type (n = 14)	1	2	1	1	0	2	0	1	2	2	0	0
Lymphangitic spread type (n = 6)	1	0	1	0	1	1	1	0	2	1	0	0
Pleural dissemination type (n = 4)		(–)			(–)			(–)			(–)	
Lobar replacement type (n = 3)	2	0	0	0	1	0	0	1	0		(–)	
Air-space consolidation type (n = 2)		(–)			(–)			(–)			(–)	
Total (n = 68)	7	8	7	2	5	11	2	3	6	5	2	0

Grade 1 = mild luminal stenosis with wall irregularity; grade 2 = moderately compressive stenosis; grade 3 = severe constrictive stenosis or luminal invasion.

The pleural effusion and pericardial effusion were observed in 31 (45.6%) and 14 (20.6%) cases, respectively. Intratumoral calcification was observed only in 2 cases. The margin of the primary tumor in the lung field was almost clear and well demarcated in the peripheral, peripheral + mediastinal extension, and pleural dissemination types. They appeared as spherical or slightly lobulated nodular shadows with no air-bronchogram (Fig. 4A, B). They were heterogeneously enhanced with intravenous contrast material. Nonenhanced necrotic or cystic changes constitute a small part. The convergence of surrounding pulmonary blood vessels or pleural indentation was not conspicuous (Fig. 4B). The surgically resected specimens showed clearly defined white to tan mass as demonstrated in Figure 4C. The histologic examination revealed nests and sheetlike cohesive aggregate of carcinoma cells with hyperchromatic nuclei and nuclear molding (Fig. 4D). In some areas, massive necrotic change and invasion of blood vessel walls in the mass lesions were observed.

The neuron-specific enolase (NSE) and gastrin releasing peptide precursor (ProGRP), which are relatively specific serum tumor markers for SCLC[15,16] were elevated in many cases.

DISCUSSION

In our study subjects, the most common type of the spreading patterns was the central+ mediastinal extension type (n = 20 [29.4%]). So, we can estimate that it is not difficult for SCLC to extend to the contralateral mediastinal tissue. The central perihilar type corresponding to the classical form of early SCLC which confined in ipsilateral hilar/mediastinum tissue was observed in 12 cases (17.6%). The peripheral type and the peripheral + mediastinal extension type were relatively frequently observed in 10.3% (7/68) and 22% (15/68), respectively. The frequency (32.4% [22/68]) of SCLC occurring in the peripheral lung is higher than previously reported.[4,5,17] We estimated this form of SCLC is not rare as previously supposed. One reason is that we could clearly observe the peripheral lung field without any slice gap due to the improvements in resolution and CT techniques.

Atypical extension forms, such as lymphangitic spread type, pleural dissemination type, lobar replacement type, air-space consolidation type, were presented in 15 of the 68 SCLC cases (22%) (Table 1). To our knowledge, pneumonialike air-space infiltrative spread type of SCLC has not been described before (Fig. 7A–C). But in some kinds of neoplastic lung diseases, such as bronchiolo-alveolar cell carcinoma, mucosa associated lymphoid tissue lymphoma, the consolidation type has been reported before.[18,19] When its margin was indistinct and peripheral ground glass opacity was associated, we considered that this consolidation shadow reflected the infiltration of tumor cells growing with nest formation filling alveolar air spaces with or without alveolar hemorrhage. In this infiltrative shadow, cystic air lucent area was observed (Fig. 7C). These air containing spaces were thought to be representing with the necrotic portion or underlying the emphysematous lung. In contrast with bronchiolo-alveolar cell carcinoma or mucosa associated lymphoid tissue lymphoma, relatively stenotic change of pulmonary vessels was demonstrated in our SCLC cases. We thought this phenomenon was caused by angio-invasive nature of SCLC. The centrilobular nodular or branching shadows which usually represent bronchogenic spread of inflammation were not observed. In the study subjects, multiple liver metastases were already presented when the diagnosis of SCLC was made by sputum cytology or histology. We also observed the elevation of relatively specific tumor marker NSE and the diminishment of infiltrative shadows were seen after the chemotherapy. In this case, histologic correlation was not obtained. However, we thought this infiltrative shadow could be distinguished from a postobstructive pneumonia because the laboratory data did not show the elevation of the C-ractive protein nor leukocytosis.

We consider the tumor of SCLC could easily spread via the lymphatic system in the bronchovascular bundle (Fig. 4), interstitial space and pleura. In the lobar replacement type

(Fig. 6), the tumor delineated by interlobar fissure grew to the almost entire 1 lobe. This was different from lobar atelectasis at 2 points: (1) affected lobe did not show the volume loss, (2) neither air bronchogram nor mucoid impaction reflecting residual bronchial tree was observed. Probably due to the severe invasion to the pulmonary vessel, opacified pulmonary vessels in the mass lesion were not apparent on CE-CT. The degree of enhancement was not marked probably due to relatively ischemic blood supply and tumor necrosis. Massive bilateral peribronchial lymphadenopathy enclosed SVC in which central venous line catheter was placed. These findings revealed that tumor growth was aggressive and widely but could be blocked with pleural membrane to some extent. No apparent gross chest wall invasion exceeding parietal pleura was observed in this study.

SCLC is strongly associated with smoking history.[1–3] In most of the cases, they arise in the main stem or lobar bronchus. The tumor tends to grow in the bronchial submucosa and subsequently invades the peribronchial connective tissues.[2–5] The stenosis of trachea to subsegmental bronchial branch caused by peribronchial extension was frequently seen in our study subjects as shown in Table 1. By using coronal reconstructive images scanned by MDCT such as Figure 2C, its peribronchial submucosal extension was clearly shown with almost preservation of bronchial inner wall. Postobstructive pneumonia or atelectasis was rarely observed because of its less obstructive change compared with other central tumor such as squamous cell carcinoma.

We also encountered many (30/68 [44.1%]) cases in which the great vessel walls, such as SVC or PA, were involved by the tumor and mediastinal adenopathy or invaded by the tumor itself (SVC, 22 cases [32.3%]; main PA, 18 cases [26.4%]; main PV, 11 cases [16.1%]) (Tables 1, 2). Severe constrictive stenosis or direct invasion into the lumen of the blood vessel such as SVC (Figs. 2A, 3), main PA (Fig. 2B), and main PV were assessed to be present in 7 (10.3%), 11 (16.1%), 6 (8.8%) cases, respectively (grade 3 stenosis). Mild luminal stenosis with wall irregularity and moderately compressive stenosis of SVC in whom we suspected tumor penetration into the adventitia were seen in 7 (grade 1) and 8 cases (grade 2), respectively.

Tumor involvement of the thoracic aortic wall was also observed in 7cases. In some cases, intravenous thromboses were also observed in SVC or brachiocephalic vein. We thought these angio-invasive natures were relatively specific features of SCLC.

We observed many cases with compressive deformity of the heart. Among them, we diagnosed the tumor extension into the intra-(n = 2) and pericardium (n = 8) by the CT findings of the tumor extension to the left atrium of the heart or irregular thickening of the pericardium. As reported before,[13] lung cancer could extend to the intrapericardium space and/or heart such as left atrium via PV. Therefore, we thought cardiac involvement of SCLC was not unusual phenomenon. But there is no definite evidence in this regard because no intracardiac biopsy was performed in our study. So, further studies were necessary.

The tumor was ill-defined in the central and mediastinal extension type because of conglomeration with lymph node metastasis or mediastinal connective tissue. On the other hand, the margin of the primary tumor in the lung field was almost clear and well demarcated in the peripheral, peripheral + mediastinal extension, and pleural dissemination types. They appeared as spherical or slightly lobulated nodular shadows with no air-bronchogram (Fig. 4A, B). They were heterogeneously enhanced with intravenous contrast material. Non-enhanced necrotic or cystic changes constitute a small part. The convergence of surrounding pulmonary vessels or pleural indentation was not conspicuous (Fig. 4B).The surgically resected specimens showed clearly defined white to tan mass and histologic examination revealed tumor cells tended to grow forming clusters or nests in the peripheral alveoli. The adjacent tissue reaction, such as inflammation or desmoplastic reaction, was not marked (Fig. 4D). Probably due to the scarce inner fibrotic change, pulmonary vessel-convergence or pleural-indentation was not obvious on CT.

Small cell lung carcinoma is a rapidly progressive tumor characterized by lymph node and distant organ metastases even at the time of first consultation. In 65 of 68 cases, lymph node metastases were observed in this study. As previously described, distant metastases to extrapulmonary organs were frequently observed (Table 1).[1–6] So, it is better to consider SCLC as a systemic disease rather than regional malignancy. Fortunately, the results of many new therapy regimens have improved.[20,21]

Our study has several limitations. First, complete radiologic and pathologic correlation was performed only in 7 cases. So, all nodular shadows or mass lesion and bulky lymphadenopathy were not confirmed to represent tumor foci or metastatic invasion even if in clinically suspected multiple metastases. Second, CT studies have limitations in regard to the staging of lymph node disease.[22,23] Third, CT imaging which can evaluate gross invasion to the mediastinal and chest wall has limited accuracy when invasion is subtle.[24,25] Therefore, further study should be performed on more patients including autopsied patients with histologically proven SCLC. PET or fused PET/CT correlative study was also necessary.

In conclusion, we observed 8 types of the tumor extension pattern of SCLC. They could be grouped into common and relatively rare types: namely, common types (central perihilar type, central + mediastinal extension type, peripheral type, and peripheral + mediastinal extension type) and relatively rare types (lymphangitic spread type, pleural dissemination type, lobar replacement type, and air-space consolidation type) (Table 1 and Fig. 1). We also found characteristic CT findings of SCLC; namely, peribronchial mainly submucosal extension and highly invasive nature to the cardiovascular system such as SVC, PA, PV, pericardium, and heart. The contour of the primary tumor in the lung field was well demarcated round to slightly lobulated without surrounding vascular convergence.

REFERENCES

1. Simon GR, Wagner H. Small cell lung cancer. *Chest*. 2003;123 (Supplement 1):259–271.
2. JD Minna, Rosenberg, eds. Cancer: Principals and practice of oncology. VOL3JB Lippincott; 1989:591–705.
3. Colby TV, Koss MN, Travis WD. Carcinoma of the lung: Overview,

incidence, etiology and screening. In: *Atlas of Tumor Pathology. Tumors of the Lower Respiratory Tract.* DC Washington: Armed Forces Institute of Pathology; 1995:91–106.
4. Pearlberg JL, Sandler MA, Lewis JW, et al. Small-cell bronchogenic carcinoma: CT Evaluation. *AJR.* 1988;150:265–268.
5. Whitley NO, Fuks JZ, McCrea ES, et al. Computed tomography of the chest in small cell lung cancer: potential new prognostic signs. *AJR.* 1984;141:885–892.
6. Norlund JD, Byhardt RW, Foley WD, et al. Computed tomography in the staging of small cell lung cancer: implications for combined modality therapy. *Int J Rad Oncol Biol Phys.* 1985; 11:1081–1084.
7. Bonner JA, Sloan JA, Shanahan TG, et al. Phase III comparison of twice-daily split-course irradiation versus once-daily irradiation for patients with limited stage small cell lung carcinoma. *J Clin Oncol.* 1999;17:681–2691.
8. Noda K, Nishiwaki Y, Kawahara M, et al. Randomized phase III study of irinotecan (CPT-11) and cisplatin versus etoposide and cisplatin in extensive disease small cell lung cancer: Japan Clinical Oncology Group study. *Proc Am Soc Clin Oncol.* 2000;19:483a.
9. Jung BC, Choong KP, Dong WP, et al. Does contrast enhancement on CT suggest tumor response for chemotherapy in small cell carcinoma of the lung? *J Comput Assist Tomogr.* 2002;26(5):797–800.
10. Mountain CF, Carr DT, Anderson WA. A new international staging system for lung cancer. *Chest.* 1986;89:225S–235S.
11. Mountain CF. Revisions in the international system for staging lung cancer. *Chest.* 1997;111:1710–1717.
12. Cymbalista M, Waysberg A, Zacharias C, et al. CT demonstration of the 1996 AJCC-UICC regional lymph node classification for lung cancer staging. *Radiographics.* 1999;19:899.
13. Munk PL, Muller NL, Miller RR, et al. Pulmonary lymphangitis carcinomatosis: CT and pathologic findings. *Radiology.* 1988;166:705–709.
14. Choe EH, Lee JH, Kim KH, et al. Obliteration of the pulmonary vein in lung cancer: Significance in assessing local extent with CT. *J Comput Assist Tomogr.* 1998;22:587–591.
15. Schneider J, Philipp M, Salewski L, et al. Pro-gastrin releasing peptide (ProGRP) and neuron specific enolase (NSE) in therapy control of patients with small cell lung cancer. *Clin Lab.* 2003;49:35–42.
16. Oremek GM, Sapoutzis N. Pro-gastrin releasing peptide (ProGRP), a tumor marker for small cell lung cancer. *Anticancer Res.* 2003; 23:895–898.
17. Cohen MH, Matthews ML. Small cell bronchogenic carcinoma: a distinct clinicopathologic entity. *Semin Oncol.* 1978;5:234–243.
18. Adler B, Padley S, Miller RR, et al. High resolution CT of bronchioalveolar carcinoma. *Am J Roentogenol.* 1992;159:275–277.
19. Wislez M, Cadranel J, Antoine M, et al. Lymphoma of pulmonary mucosa-associated lymphoid tissues: CT scan findings and pathological correlations. *Eur J Respir.* 1999;14:423–429.
20. Pignon JP, Arriagada R, Ihde DC, et al. A meta-analysis of thoracic radiotherapy for small cell lung cancer. *N Engl J Med.* 1992;327:1618–1624.
21. Shields TW, Higgins GA, Mathew MJ, et al. Surgical resection in the management of small cell carcinoma of the lung. *J Thoracic Cardiovasc Surg.* 1982;84:481–488.
22. Dales RE, Stark RM, Raman S. Computed tomography to stage lung cancer: approaching a controversy using meta-analysis. *Am Rev Respir Dis.* 1990;141:1096–1101.
23. Dwamena BA, Sonnad S, Angobaldo S, et al. Metastases from non-small cell lung cancer. Mediastinal staging in the 1990's: meta-analytic comparison of PET and CT. *Radiology.* 1999;213:530–536.
24. Martini N, Heelan R, Westcott J, et al. Comparative merits of conventional, computed tomographic, and magnetic resonance imaging in assessing mediastinal involvement in surgically confirmed lung carcinoma. *J Thoracic Cardiovasc Surg.* 1985;90:639–648.
25. Padovani B, Mouroux J, Seksik L, et al. Chest wall invasion by bronchogenic carcinoma: evaluation with MR imaging. *Radiology.* 1993;187:33–38.

